energies

MDPI

Article

# A Novel Partial Discharge Detection Method Based on the Photoelectric Fusion Pattern in GIL

**Yiming Zang [1], Yong Qian [1], Wei Liu [2], Yongpeng Xu [1,*], Gehao Sheng [1] and Xiuchen Jiang [1]**

[1] Department of Electrical Engineering, Shanghai Jiao Tong University, 800 Dongchuan Road, Minhang, Shanghai 200240, China; zangyiming@sjtu.edu.cn (Y.Z.); qian_yong@sjtu.edu.cn (Y.Q.); shenghe@sjtu.edu.cn (G.S.); xcjiang@sjtu.edu.cn (X.J.)

[2] Key Laboratory for Sulfur Hexafluoride Gas Analysis and Purification of SGCC, Anhui Electric Power Research Institute of SGCC, Hefei 230022, China; sgccliu@163.com

* Correspondence: xyp3525@sjtu.edu.cn; Tel.: +86-155-0211-2557

Received: 25 September 2019; Accepted: 27 October 2019; Published: 28 October 2019


**Abstract:** Optical detection and ultrahigh frequency (UHF) detection are two significant methods of partial discharge (PD) detection in the gas-insulated transmission lines (GIL), however, there is a phenomenon of signals loss when using two types of detections to monitor PD signals of different defects, such as needle defect and free particle defect. This makes the optical and UHF signals not correspond strictly to the actual PD signals, and therefore the characteristic information of optical PD patterns and UHF PD patterns is incomplete which reduces the accuracy of the pattern recognition. Therefore, an image fusion algorithm based on improved non-subsampled contourlet transform (NSCT) is proposed in this study. The optical pattern is fused with the UHF pattern to achieve the complementarity of the two detection methods, avoiding the PD signals loss of different defects. By constructing the experimental platform of optical-UHF integrated detection for GIL, phase-resolved partial discharge (PRPD) patterns of three defects were obtained. After that, the image fusion algorithm based on the local entropy and the phase congruency was used to produce the photoelectric fusion PD pattern. Before the pattern recognition, 28 characteristic parameters are extracted from the photoelectric fusion pattern, and then the dimension of the feature space is reduced to eight by the principal component analysis. Finally, three kinds of classifiers, including the linear discriminant analysis (LDA), support vector machine (SVM), and k-nearest neighbor (KNN), are used for the pattern recognition. The results show that the recognition rate of all the photoelectric fusion pattern under different classifiers is higher than that of optical and UHF patterns, up to the maximum of 95%. Moreover, the photoelectric fusion pattern not only greatly improves the recognition rate of the needle defect and the free particle defect, but the recognition accuracy of the floating defect is also slightly improved.

**Keywords:** partial discharge; optical-UHF integrated detection; photoelectric fusion pattern; GIL; NSCT

## 1. Introduction

In recent years, gas-insulated transmission lines (GIL) are widely used in the power transmission of hydropower stations and nuclear power plants because of their high efficiency, large transmission capacity, high reliability, and small footprint [1–3].

In the operation of GIL, partial discharge (PD) is a precursor in the deterioration of insulation performance, which is the main cause of a breakdown. In addition, the severity of PD is closely related to the type of discharge defect. Therefore, PD detection and pattern recognition are particularly important in the GIL [4,5]. In order to improve the reliability of PD detection and pattern recognition,

some scholars have proposed a method of combining the fluorescent fiber detection and the ultrahigh frequency (UHF) detection in the PD detection of gas-insulated equipment, which has the characteristics of high sensitivity, strong anti-interference ability, and wide application range [6].

Although optical-UHF integrated detection can effectively detect the occurrence of PD, optical detection and UHF detection have certain limitations for the pattern recognition of PD. UHF detection is limited by its detection bandwidth and is susceptible to influence from the external electromagnetic interference, resulting in the loss of UHF signals [7]. For optical detection, the propagation of the optical signal is affected by the structure of the GIL, the location of sensors, the distance of sensors, and the position of the PD source, which will weaken or even shield optical signals reaching the sensor. This can also result in the loss of optical signals [8]. Therefore, both UHF detection and optical detection have the phenomena of signals loss, which will lead to incomplete feature information in the PD pattern. Therefore, if the UHF pattern and the optical pattern are separately used for pattern recognition in the optical-UHF integrated detection, both detections will be affected by the pattern aliasing or the false pattern in the recognition process due to the missing information of the PD characteristic. These adverse effects will reduce the accuracy of PD pattern recognition.

In order to improve the accuracy of PD pattern recognition in the GIL, this study proposes an image fusion algorithm based on improved non-subsampled contourlet transform (NSCT) [9], which can gain the photoelectric fusion phase-resolved partial discharge (PRPD) pattern by fusing the optical PRPD pattern with the UHF PRPD pattern. By applying the photoelectric fusion PRPD pattern to the pattern recognition of PD, the two detection methods are complemented, avoiding the problem of missing PD characteristic information in a single type of the detection pattern.

Compared with the traditional NSCT method [10], the improved NSCT image fusion algorithm with the multiscale, multidirectional, and translation-invariant characteristics can retain more image edge and texture information, which can more completely contain the PD characteristic information of optical and UHF signals. In order to better characterize the PD characteristics of the PD pattern, 28 characteristic parameters, such as moment features and texture features, are extracted from the photoelectric fusion PD pattern and, then, the principal component analysis (PCA) method is used to reduce the feature vector space to eight characteristic parameters. After the process of PCA, linear discriminant analysis (LDA), support vector machine (SVM), and k-nearest neighbor (KNN) were used to verify the pattern recognition accuracy by photoelectric fusion patterns. Therefore, through the method of photoelectric image fusion, it provides a novel idea for the optical-UHF integrated detection of PD.

## 2. PD Experiment of GIL

### 2.1. Experimental Platform and Defect Model

The GIL experimental platform used in this study is shown in Figure 1. In order to isolate external electromagnetic interference, the whole experimental platform is located in the metal shielded room. In the platform, the GIL test tank is made of aluminum alloy, and the seal is good without light injection. The photoelectric integrated sensor that is composed of a fluorescent fiber intertwined on the cylindrical UHF detection is installed on the tank wall for PD signals acquisition. The detection frequency band of the UHF sensor is 300–500 MHz. The photomultiplier tube (PMT) adopts the HAMAMATSU-H10722-01 model whose corresponding range of spectrum is 230,920 nm, and the voltage/current conversion coefficient is 1V/μA. The function of PMT is to convert the collected optical signals into electrical signals, which is helpful for signal processing. The digital PD detector (Haffley DDX 9121b) collects standard PD signals as a reference to confirm the loss of optical signals and UHF signals. The oscilloscope uses LeCroy-HDO6000A [11].

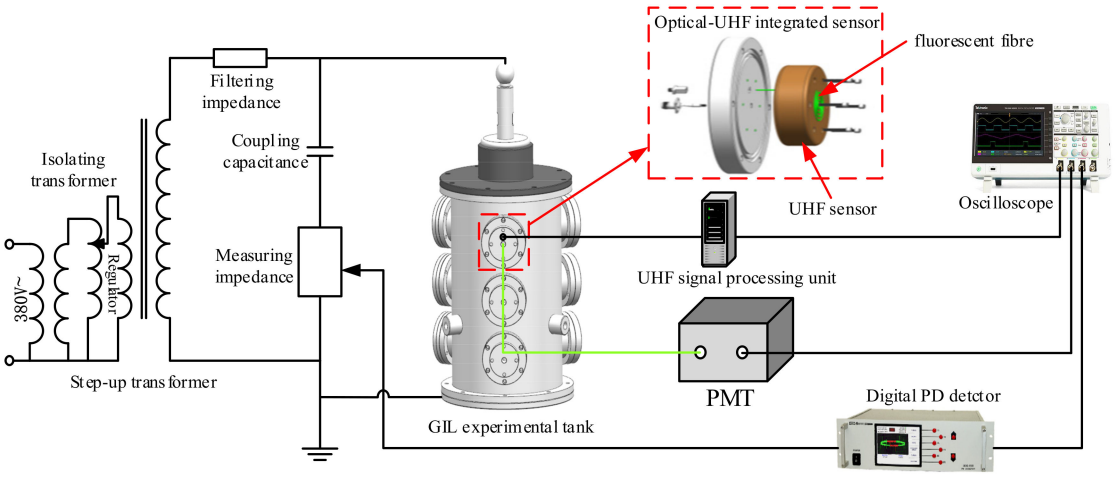


**Figure 1.** Partial discharge (PD) detection platform of gas-insulated transmission lines (GIL).

In order to simulate the PD defects in GIL, Figure 2 shows three aluminum typical defect models of the needle discharge defect, the floating discharge defect, and the free particle discharge defect designed in this study [12].

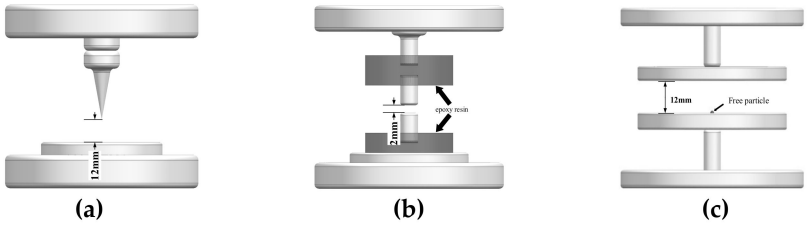


**Figure 2.** Schematic diagram of three insulation defect models. (**a**) The needle discharge defect, (**b**) the floating discharge defect, and (**c**) the free particle discharge defect.

## 2.2. Experimental Method

Before the experiment, PD defects and the tank were dedusted. The $SF_6$ gas was then filled into the GIL experimental tank that was sealed and vacuum until the gas pressure reached 0.2 MPa. According to the above operation, three typical PD defects were placed into the GIL experimental tank for PD experiments. During the experiment, the center of the optical-UHF integrated sensor was facing the defect on the level.

For the data acquisition, PD detection was performed for each defect at several voltage levels. For each defect, 120 detection samples were collected and each sample included 50 PD signals of a power frequency cycle.

## 2.3. Analysis of the Experimental Results

According to the time domain waveform of Figure 3, comparing the UHF signals and optical signals with the PD detector signals that act as the standard signals confirms that the signal loss is relative to the detection method and discharge defects, rather than external signal interference.

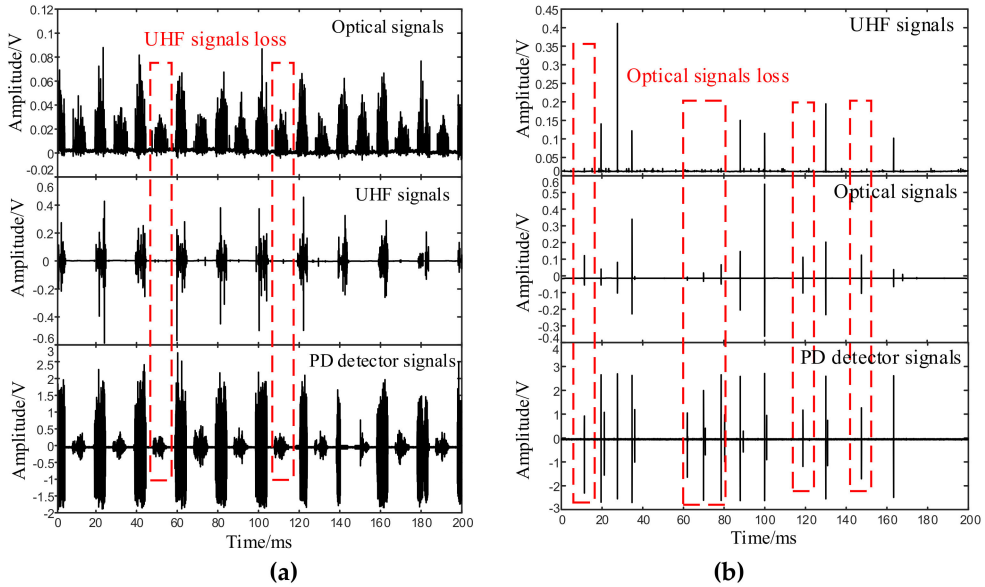


**Figure 3.** Optical and ultrahigh frequency (UHF) PD signals with different defects. (**a**) Time domain waveform of needle defect and (**b**) time domain waveform of free particle defect.

In the UHF detection, the sensitivity of the UHF detection is low due to the limitation of the detection band and the interference of the environmental noise. Thereby, it is shown that the PD detection of the needle discharge defect has a phenomenon of UHF signal loss in the experiment.

In the optical detection, the uncertainty of the free particle discharge is strong, and the intensity of the free particle discharge is not uniform. In addition, the optical detection is easily affected by the photon propagation path and the reflection condition of GIL inner wall. Therefore, the PD detection of the free particle discharge also has a phenomenon of optical signal loss.

In order to represent the characteristic information of PD more effectively, this study uses the two-dimensional PRPD pattern to describe the phase information of PD. The PRPD pattern is represented by a $\varphi$–$u$ two-dimensional pattern, where $\varphi$ represents the power frequency phase at which PD occurs and $u$ represents the intensity of PD signals [13]. The color of the PRPD pattern represents the discharge density at certain phase and amplitude, which is shown by the color bar. Each PRPD pattern is drawn from a PD signal sample, including 50 PD cycles acquired by the oscilloscope above, which can guarantee that the loss of signal is not an accident.

For the needle defect, the PRPD pattern of the optical-UHF integrated sensor at 20 kV is shown in Figure 4. Optical signals are mainly concentrated near the peaks of positive and negative half cycles, while most UHF signals appear only in the area of the negative half cycle. It can be concluded that the detection sensitivity of the UHF sensor is lower than that of the optical sensor. When the PD intensity of the positive half cycle is small, the UHF sensor cannot detect the PD signals. Therefore, there is a phenomenon of missed UHF signals in the positive half cycle, which can cause the PD characteristic information to be incomplete and interfere with the PD pattern recognition.

For the floating defect, as shown in Figure 5, optical signals and UHF signals are mainly distributed near the peak of the positive and negative half cycles at 20 kV, which has good distribution characteristics of phase concentration. Therefore, the optical and UHF PD signals collected by the optical-UHF integrated sensor has good correspondence.

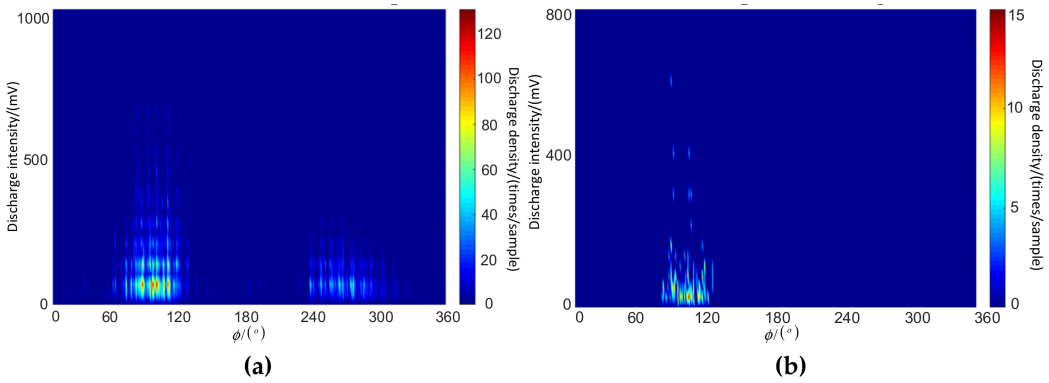


**Figure 4.** Phase-resolved partial discharge (PRPD) patterns of the needle defect under 20 kV. (**a**) A PRPD pattern of the optical detection and (**b**) a PRPD pattern of the UHF detection.

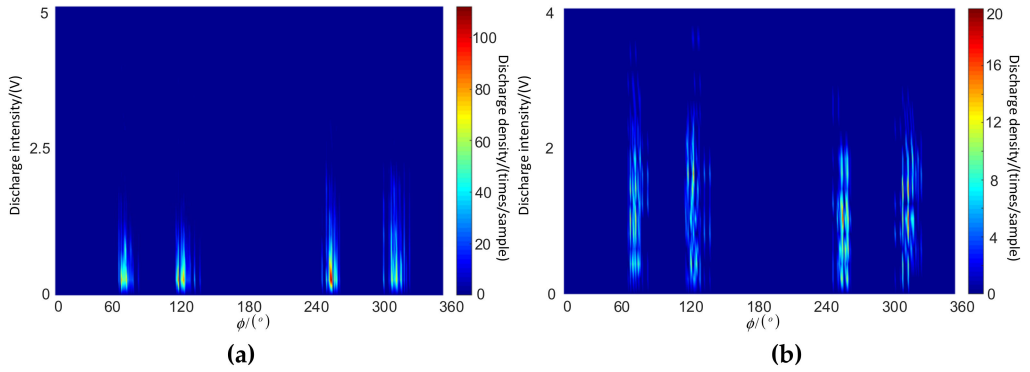


**Figure 5.** PRPD patterns of the floating defect under 20 kV. (**a**) A PRPD pattern of the optical detection and (**b**) a PRPD pattern of the UHF detection.

For the free particle defect, the PRPD pattern of the optical-UHF integrated sensor at 20 kV is shown in Figure 6. Under the action of the electric field force, the free metal particle undergo random collision movement between the plates and the discharge repetition rate of it is low, which causes the phase distribution of UHF signals to be relatively random in the PRPD pattern. It can be seen from the optical pattern that the randomness of the optical signal distribution is weak. The light spots in the optical pattern are mainly concentrated in the negative half cycle, instead of being distributing randomly. Therefore, the distribution of optical signals has a large difference from the UHF signal pattern. It is indicated that optical signals are attenuated by the occlusion and the reflection phenomenon of the propagation path during the propagation process, which causes optical signals to be missed and incompletely collected [8]. As a result, the loss of PD information leads to a failure to fully represent the PD characteristics of the free particle defect.

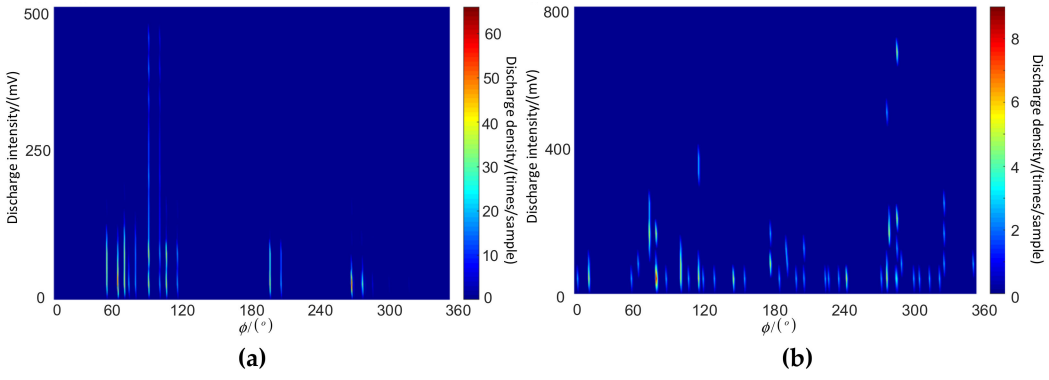


**Figure 6.** PRPD patterns of the free particle defect under 20 kV. (**a**) A PRPD pattern of the optical detection and (**b**) a PRPD pattern of the UHF detection.

The above experiments prove that the PD characteristic information of UHF and optical PRPD patterns is incomplete. The UHF sensor has the loss of signals on the needle defect, and the optical sensor has the loss of signals on the free particle defect. Therefore, if the two types (UHF patterns and optical patterns) of PRPD patterns are separately used for pattern recognition, the lack of the characteristic information may result in a decrease in recognition accuracy.

## 3. Image Fusion Algorithm Based on Improved NSCT

### *3.1. NSCT Structure*

For PD patterns, the edge texture plays a key role in identifying the type of PD. Therefore, this study uses an image fusion algorithm based on the improved NSCT method to fuse the optical pattern with the UHF pattern. Its structure can be divided into two parts, non-subsampled pyramid filter banks (NSPFB) and non-subsampled directional filter bank (NSDFB). The structural framework of the NSCT is shown in Figure 7.

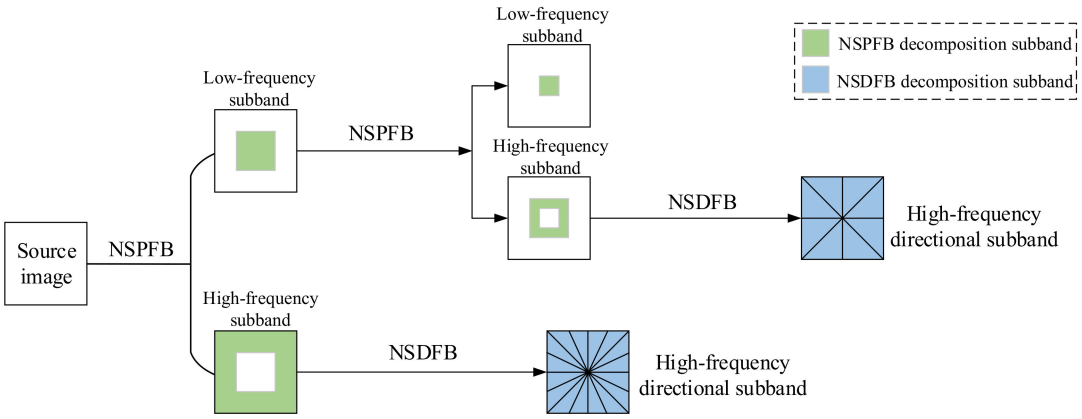


**Figure 7.** Structure block diagram of non-subsampled contourlet transform (NSCT) decomposition.

NSPFB is used as a filter that is up sampled. In order to achieve multiscale decomposition of the image, NSPFB performs up-sampling processing by the matrix $D = 2I$ iteratively, which can obtain the filter $H(Z^{2I})$. The NSPFB filters the low-frequency subband image of the upper level by the lowpass filter $H_0(Z^{2I})$ and the bandpass filter $H_1(Z^{2I})$, so that each level is decomposed into a low-frequency subband image and a high-frequency subgraph. The definition of the decomposition scale is $j$. In the filtering process, the ideal frequency domain of the lowpass filter at $j$ scale is $[-\pi/2j, \pi/2j] \times [-\pi/2j, \pi/2j]$. The corresponding ideal frequency domain of the bandpass filtering is $[-\pi/2j + 1, \pi/2j + 1] \times [-\pi/2j-1, \pi/2j-1]$ [14]. Thus, after the image is decomposed by the $j$-level NSPFB, the image can obtain $j + 1$ subgraph of the same size as the original decomposition image, including one low-frequency subgraph and $j$ high-frequency subgraph. Taking the three-level NSPFB decomposition as an example, its structure is shown in Figure 8 [15].

The NSDFB used in the NSCT is based on a fan-shaped filter bank. The two-channel directional filters, $U_0(Z)$ and $U_1(Z)$, with the fan-shaped frequency domain are up-sampled by the sampling matrix $D$ to obtain filters $U_0(Z^D)$ and $U_1(Z^D)$. Then $U_0(Z^D)$ and $U_1(Z^D)$ are used to filter the subgraph decomposed in the upper level, which can achieve more accurate directional decomposition of the image in the image of corresponding frequency domain. As shown in Figure 9, taking the two-level directional decomposition as an example, the NSDFB decomposes the two-dimensional frequency domain into several wedge-shaped regions representing directionality [16]. Each wedge-shaped region contains detailed direction features of the image. Therefore, by performing $k$-level directional decomposition on the subgraph at one level of the NSPFB, it is possible to obtain a $2^k$ directional subgraph with the same size as the source image [17].

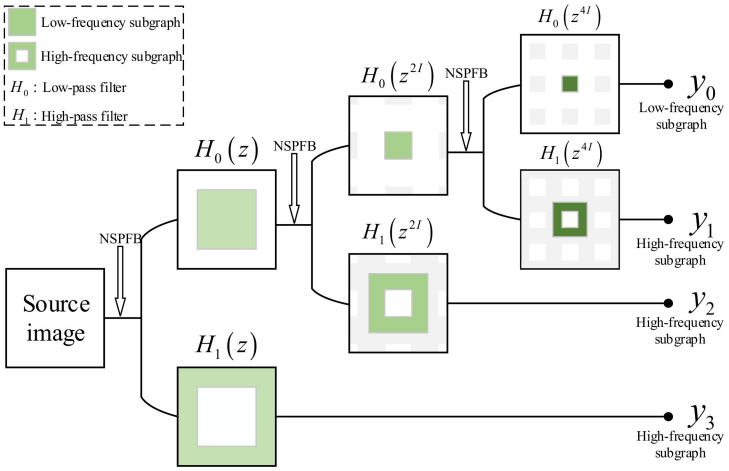


**Figure 8.** Three-level NSPFB pyramid filter bank.

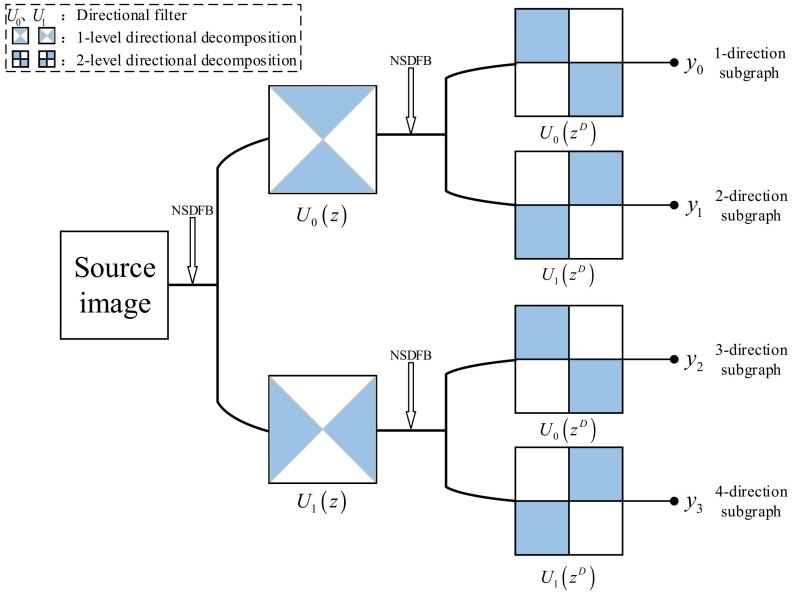


**Figure 9.** Two-level NSDFB directional filter bank.

### *3.2. Improved Image Fusion Rules Based on NSCT*

According to the NSCT decomposition above, when $k_j$ represents the NSDFB directional decomposition levels of the image on the $j$th-level of the J-level NSPFB decomposition, the number of subgraph generated by the decomposition can be expressed as $1+\sum_{j=1}^{j} 2^{k_j}$, including one low-frequency subgraph and $\sum_{j=1}^{j} 2^{k_j}$ high-frequency subgraph. In order to ensure the anisotropy in the NSCT image fusion process, we change the $k_j$ on each level of the NSPFB, which can make high-frequency subgraph on each level of the NSPFB have different directional decomposition. The structural flow of image fusion is shown in Figure 10 [18].

The source images A and B are subjected to grayscale processing before the NSCT conversion. By performing NSCT decomposition on the grayscale images of the source images A and B, the high-frequency subband coefficients, $G_{j,r}^{A}(x,y)$, $G_{j,r}^{B}(x,y)$, and the low-frequency subband coefficients, $L_{J}^{A}(x,y)$, $L_{J}^{B}(x,y)$, of each source image can be obtained. Among them, $j=(1,2,\ldots,J)$ is the number of decomposition levels of the NSPFB, $r$ is the $r$th-direction of the NSDFB decomposition on the $j$th-level ($r=1,2,\ldots,2^{k_j}$), and the subband coefficient represents the gray value at location $(x,y)$.

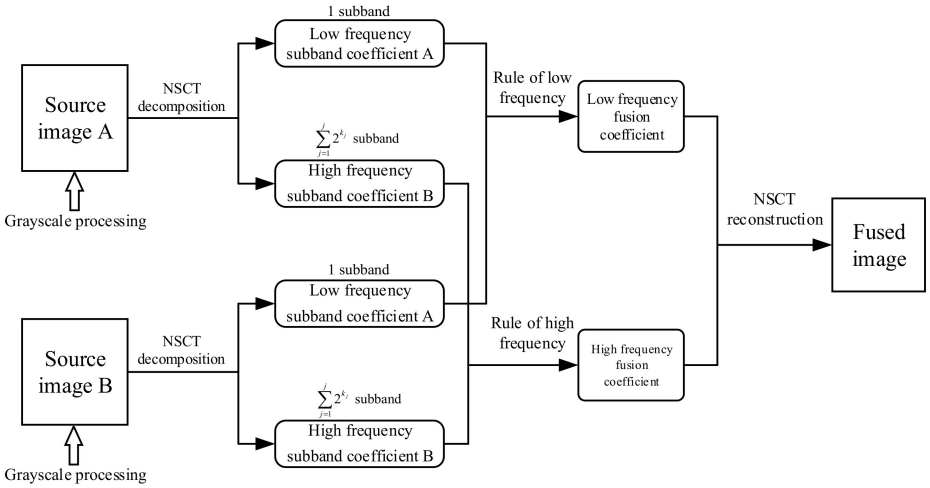


**Figure 10.** NSCT image fusion structure.

### 3.2.1. Fusion Rule of Low-Frequency Subgraph

After being decomposed by the NSCT, the contour information of the source image is mainly retained in the low-frequency subgraph. For the PRPD pattern, the contour of PD signals distribution is especially important for pattern recognition. Image fusion of the decomposed low-frequency subgraph is to preserve the contour feature information of the PRPD pattern as completely as possible. Therefore, we proposes a fusion rule of low-frequency subgraph, combining Canny operator and local entropy to better preserve the contour information of the PRPD pattern.

It is known that $L_J^A(x,y)$ and $L_J^B(x,y)$ are two low-frequency subgraphs to be fused, which are the same size. First, the low-frequency subgraph is edge-extracted by the Canny operator to obtain the edge contour binary graphs, $L_{J,Canny}^A(x,y)$ and $L_{J,Canny}^B(x,y)$. Thereby, the contour information of the signal distribution in the low-frequency subgraph is better preserved during the fusion process, which reduces the influence of image texture and sparseness.

In this study, we introduce the concept of image local entropy [19]. The local entropy can reflect the extent of gray dispersion of the image. In the image region with large local entropy, the gray value of this certain region is relatively uniform and contains less feature information. In the image region with small local entropy, the grayscale difference of this certain region is large and contains more feature information. Therefore, the local entropy is larger in the smooth region of the PRPD pattern, while the local entropy is smaller in the boundary contour region of the signal distribution for the PRPD pattern.

$f(x,y)$ is defined as the gray value of location $(x,y)$ in the image, then, an image of size $X \times Y$ whose local entropy $H_{f(x,y)}$ is defined as [20]:

$$H_{f(x,y)} = \sum_{x=1}^{X} \sum_{y=1}^{Y} p_{xy} lg p_{xy} \tag{1}$$

where $p_{xy}$ is the probability of gray distribution at location $(x,y)$, and its expression is as follows:

$$p_{xy} = \frac{f(x,y)}{\sum_{x=1}^{X} \sum_{y=1}^{Y} f(x,y)} \tag{2}$$

Therefore, the fusion method of low-frequency coefficient adopted in this study is summarized as:

1) The local entropy $H_{f(x,y)}^A$ and $H_{f(x,y)}^B$ at location $(x,y)$ of the edge contour binary patterns $L_{J,Canny}^A(x,y)$ and $L_{J,Canny}^B(x,y)$ are calculated by traversing the sampling window of size $3 \times 3$.

2) By comparing the magnitude of the local entropy at each location, it is determined how much the sample window contains image contour information. According to this, the fusion weight coefficients, $c_A(x,y)$ and $c_B(x,y)$, of the images, $L_J^A(x,y)$ and $L_J^B(x,y)$, are calculated.

$$c_A(x,y) = \frac{H^A_{f(x,y)}}{H^A_{f(x,y)} + H^B_{f(x,y)}} \tag{3}$$

$$c_B(x,y) = \frac{H^B_{f(x,y)}}{H^A_{f(x,y)} + H^B_{f(x,y)}} \tag{4}$$

3) According to the local entropy of the image and the fusion weight coefficient, the fused low-frequency subgraph $L_J^{fusion}(x,y)$ is calculated. The fusion rules are as follows:

$$L_J^{fusion}(x,y) = c_A \times L_J^A(x,y) + c_B \times L_J^B(x,y) \tag{5}$$

#### 3.2.2. Fusion Rule of High-Frequency Subgraph

After the NSCT decomposition, the detailed texture information of the source image is mainly retained in the high-frequency subgraph, which represents the density of PD signals. Therefore, the key point of the high-frequency subgraph fusion is to enhance the image features, making the high-frequency subgraph more informative.

In this study, phase congruency (PC) is applied to the fusion rule of high-frequency coefficient. PC analyzes the feature points of the grayscale image from the perspective of the frequency domain. The theoretical basis is that the image is subjected to Fourier transform decomposition, and then the points with the most consistent phase of each harmonic component correspond to the feature point of the image [21]. Thus, PC can measure the importance of subgraph features with a dimensionless measurement.

In the fusion of high-frequency subgraphs, the PC value can represent the sharpness of high-frequency subgraphs. Because the subgraph can be regarded as a 2D signal [22], the PC value of the subgraph at location $(x,y)$ can be calculated by Equation (6).

$$PC(x,y) = \frac{\sum_k E_{\theta_k}(x,y)}{\varepsilon + \sum_n \sum_k A_{n,\theta_k}(x,y)} \tag{6}$$

where $A_{n,\theta_k}$ is the amplitude of the $n$-th Fourier component and angle $\theta_k$, $\theta_k$ denotes the orientation angle at $k$, and $\varepsilon$ is a positive constant to offset the DC components of subgraph. In this study, the value of $\varepsilon$ is set to 0.001 [23]. $E_{\theta_k}(x,y)$ can be calculated by Equation (7).

$$E_{\theta_k}(x,y) = \sqrt{F^2_{\theta_k}(x,y) + H^2_{\theta_k}(x,y)} \tag{7}$$

where $F_{\theta_k}(x,y)$ and $H_{\theta_k}(x,y)$ can be calculated by Equations (8) and (9) respectively.

$$F_{\theta_k}(x,y) = \sum_n e_{n,\theta_k}(x,y) \tag{8}$$

$$H_{\theta_k}(x,y) = \sum_n o_{n,\theta_k}(x,y) \tag{9}$$

where $e_{n,\theta_k}(x,y)$ and $o_{n,\theta_k}$ are convolution results of subgraph at location $(x,y)$, which can be calculated by Equation (10).

$$\left[e_{n,\theta_k}(x,y), o_{n,\theta_k}(x,y)\right] = \left[I(x,y) \times M_n^e, I(x,y) \times M_n^o\right] \tag{10}$$

where $I(x,y)$ denotes the pixel value of subgraph at location $(x,y)$. $M_n^e$ and $M_n^o$ represent the even- and odd-symmetric filters of 2D log-Gabor at scale $n$ [23].

PC is a contrast invariant, which cannot reflect local contrast changes [22]. In order to compensate for the lack of PC, a measure of sharpness change (SCM) is introduced as below:

$$SCM(x,y) = \sum_{(x_0,y_0)\in\Omega_0} (I(x,y) - I(x_0,y_0))^2 \tag{11}$$

where $\Omega_0$ denotes a local window with a size of $3\times 3$ that is entered at $(x,y)$. $(x_0,y_0)$ is a pixel point in the local window of $\Omega_0$. In addition, the local SCM (LSCM) is expressed as Equation (12) to determinate the $(x,y)$ neighborhood contrast.

$$LSCM(x,y) = \sum_{a=-M}^{M}\sum_{b=-N}^{N} SCM(x+a,y+b) \tag{12}$$

where $(2M+1)\times(2N+1)$ represents the neighborhood size.

Since PC and LSCM cannot completely reflect the local luminance information, the local energy (LE) is proposed as below.

$$LE(x,y) = \sum_{a=-M}^{M}\sum_{b=-N}^{N} (I(x+a,y+b))^2 \tag{13}$$

Therefore, according to the theory mentioned above, a new activity measure (NAM) is defined using PC, LSCM, and LE to measure various aspects of subgraph information.

$$NAM(x,y) = (PC(x,y))^{\alpha_1}\cdot(LSCM(x,y))^{\beta_1}\cdot(LE(x,y))^{\gamma_1} \tag{14}$$

where $\alpha_1$, $\beta_1$, $\gamma_1$ are set to 1, 2, and 2 respectively, which are used to adjust the value of PC, LSCM, and LE in NAM [24].

After the NAM is obtained, the fused high-frequency image can be determined by the Equation (15).

$$H_j^{fusion}(x,y) = \begin{cases} H_A(x,y) & if Lmap_A(x,y) = 1 \\ H_B(x,y) & otherwise \end{cases} \tag{15}$$

where the $H_j^{fusion}(x,y)$ represents the high-frequency fused subgraph of $j$th-level, $H_A(x,y)$ and $H_B(x,y)$ are high-frequency subgraphs of source image A and B. $Lmap_i(x,y)$ is a decision map for the fusion of high-frequency subgraph, which can be calculated by Equation (16).

$$Lmap_i(x,y) = \begin{cases} 1 & if \lceil S_i(x,y)\rceil > \frac{\widetilde{M}\times\widetilde{N}}{2} \\ 0 & otherwise \end{cases} \tag{16}$$

where the $S_i(x,y)$ is calculated by Equation (17).

$$\begin{aligned} S_i(x,y) = \; & \{(x_0,y_0)\in\Omega_1 | NAM_i(x_0,y_0) \geq \max(NAM_1(x_0,y_0), \cdots, \\ & NAM_{i-1}(x_0,y_0), NAM_{i+1}(x_0,y_0), \cdots, NAM_K(x_0,y_0))\} \end{aligned} \tag{17}$$

where $\Omega_1$ denotes a sliding window with a size of $\widetilde{M}\times\widetilde{N}$, and $(x,y)$ is the center of it. $K$ is the number of source images.

According to the low-frequency and high-frequency subgraph fusion method mentioned above, the fused low-frequency and high-frequency NSCT coefficients $L_J^{fusion}(x,y)$ and $H_j^{fusion}(x,y)$ can be obtained. Then the fused fusion image $F$ can be reconstructed by inverse NSCT transformation.

## 4. Photoelectric Image Fusion PD Detection Based on Improved NSCT

### *4.1. Overall Detection Process*

In order to improve the accuracy rate of the pattern recognition, we propose an improved NSCT image fusion algorithm for the problem of missing PD signals in optical and UHF detections, that is, NSCT is used to decompose the grayscale optical and UHF PRPD patterns into low-frequency subgraphs and high-frequency subgraphs accordingly. The above fusion method is used to fuse the optical pattern with the UHF pattern to obtain the photoelectric fusion PD pattern. This pattern is then subjected to a series of processing such as feature extraction, dimensionality reduction, and pattern recognition. The overall process of the test verification is shown in Figure 11.

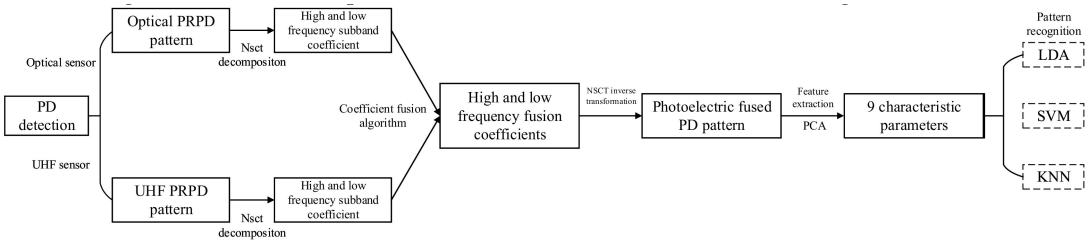


**Figure 11.** Experiment verification of the overall process.

### *4.2. Decomposition of PD Patterns Based on Improved NSCT*

On the basis of the GIL PD experimental data mentioned above, the PD of the needle defect at 20 kV is taken as an example to perform NSCT decomposition and the fusion of the PD optical pattern and the PD UHF pattern.

In the NSCT decomposition of the PRPD pattern, one low-frequency subgraph and three high-frequency subgraphs can be obtained after the three-level NSPFB decomposition. In order to ensure the anisotropy of the image decomposition and preserve the information of the image in all directions more completely, the high-frequency subgraphs on the NSPFB decomposition of the fjirst-, second- and third-level are decomposed by the NSDFB directional decomposition with $2^1$-, $2^2$-, and $2^3$-direction, respectively. Therefore, each high-frequency subgraph can be decomposed into $2^1$-, $2^2$-, and $2^3$-direction subgraphs.

As a result, $1 + \sum_{k=1}^{3} 2^k$ subgraphs that are equal in size to the original image can be obtained after the optical pattern and the UHF pattern are decomposed by the NSCT, respectively, as shown in Figures 12 and 13. It can be seen that the PD pattern is decomposed into multiscale, multidirectional high-frequency subgraphs and low-frequency subgraphs, which can retain the contour and detailed information of the source image well.

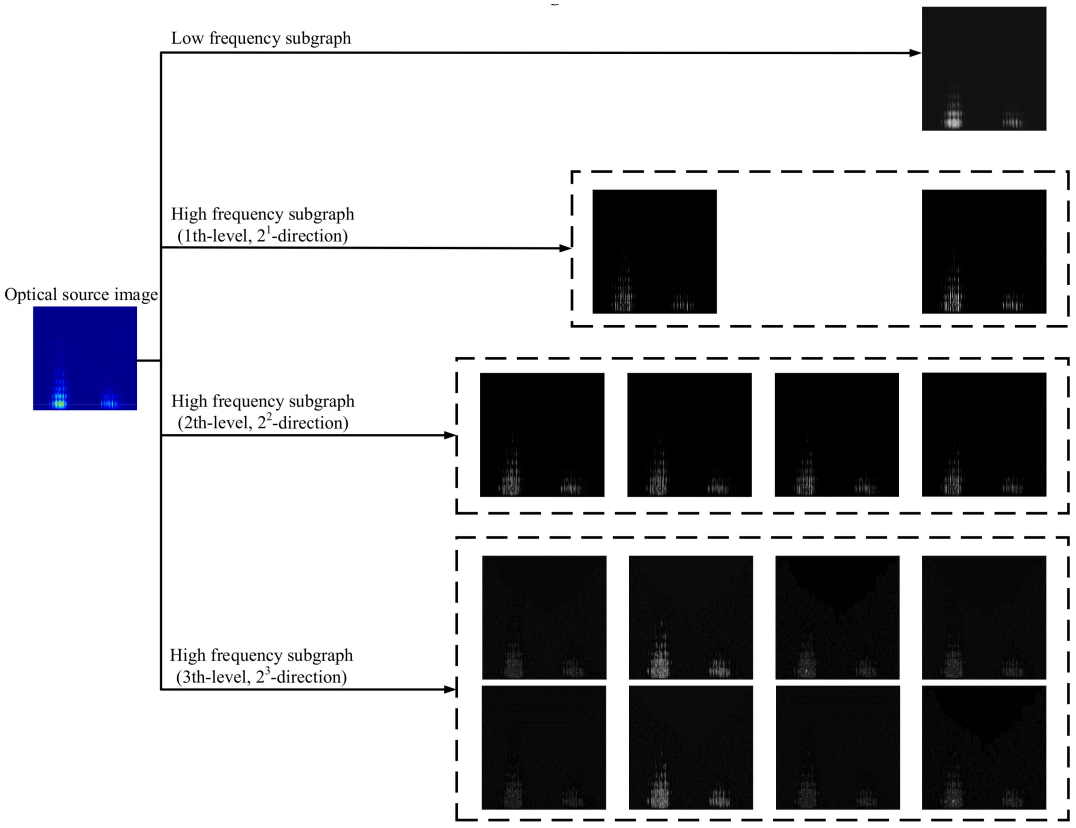


**Figure 12.** NSCT decomposition of the optical PD pattern.

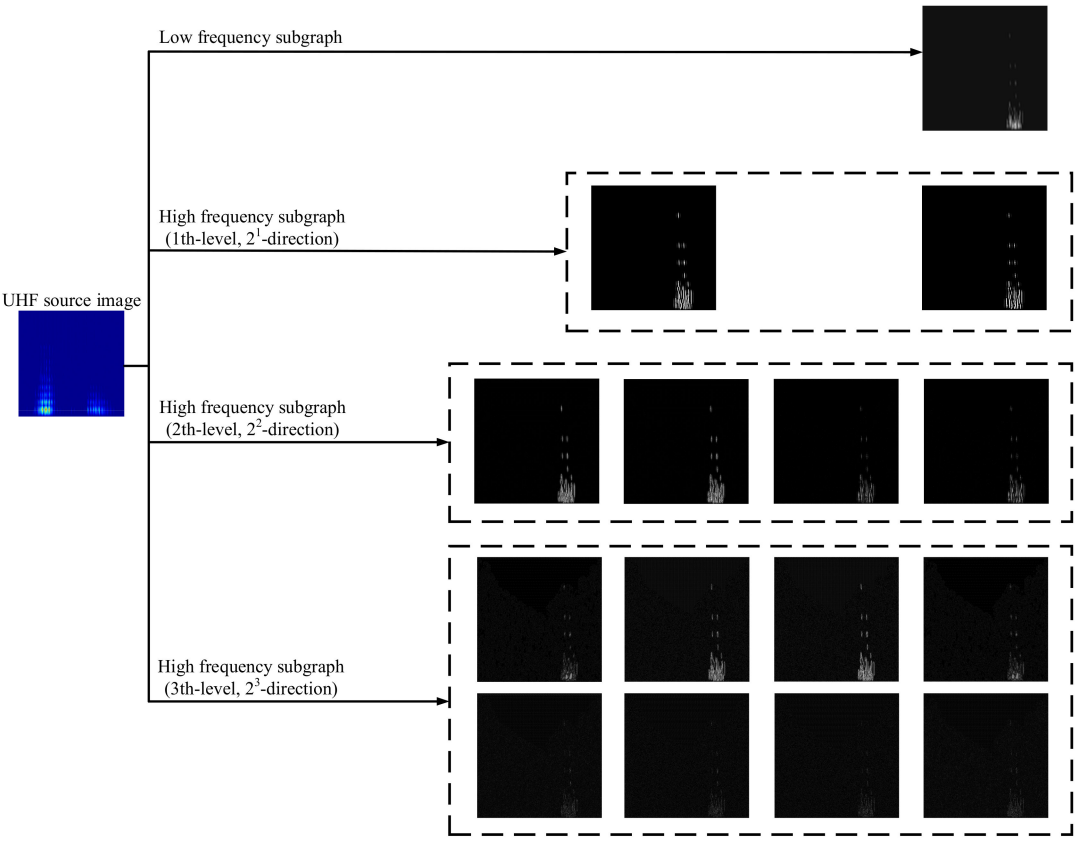


**Figure 13.** NSCT decomposition of the UHF PD pattern.

### 4.3. Fusion of the Photoelectric PD Pattern

According to the image fusion rule in Section 3.2., the corresponding fusion rule is performed on each of the low-frequency subgraph and the high-frequency subgraph, respectively, which can obtain one low-frequency photoelectric fusion subgraph and $\sum_{k=1}^{3} 2^k$ high-frequency photoelectric fusion subgraphs, as shown in Figure 14. The inverse NSCT transform is performed on the fused photoelectric subgraph to obtain a photoelectric fusion PD pattern, as shown in Figure 15.

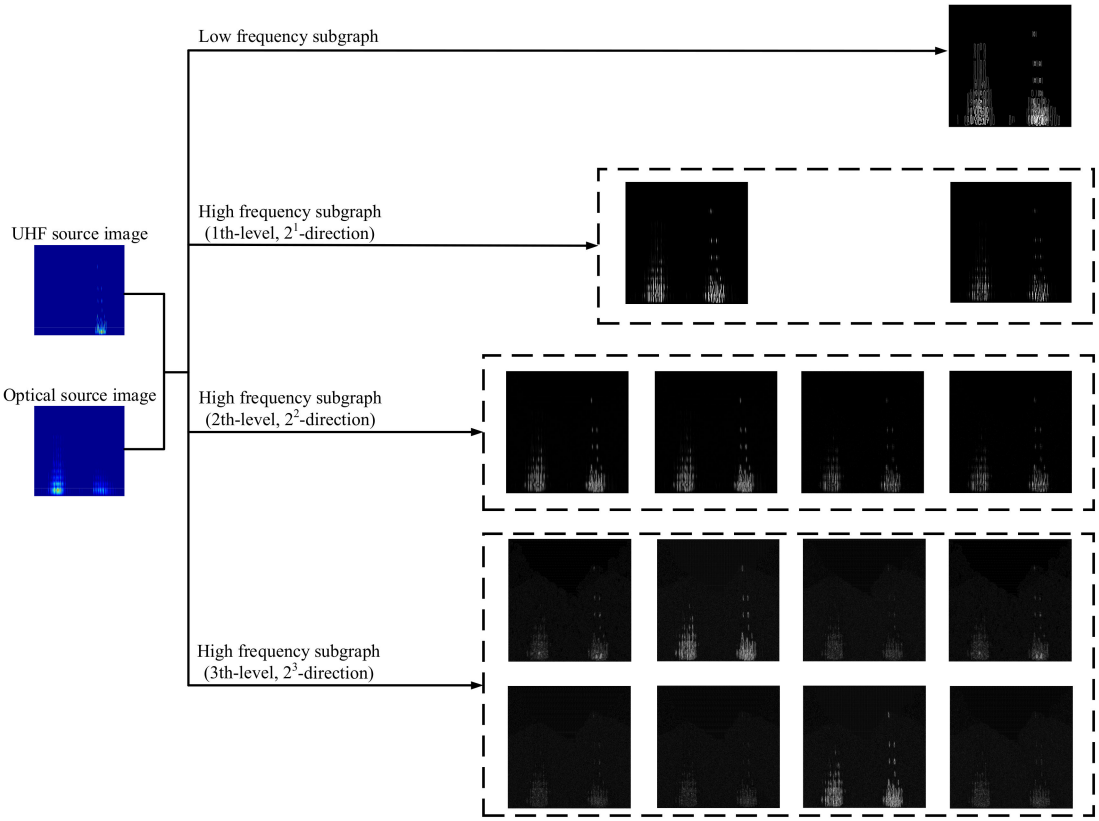


**Figure 14.** Fusion framework of optical and UHF patterns.

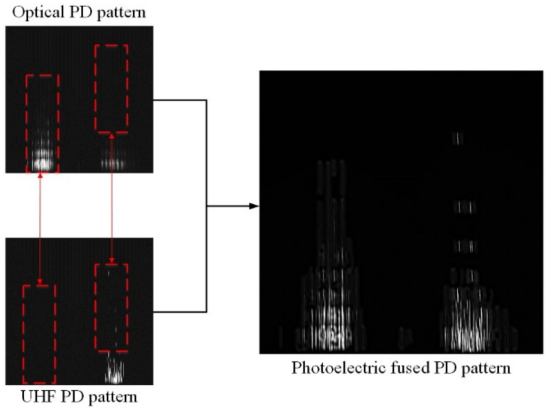


**Figure 15.** Photoelectric fusion PD pattern.

### 4.4. Feature Extraction and Dimension Reduction

In order to effectively reflect the image features, the feature parameters of the photoelectric fusion PD pattern are extracted. In this study, the eigenvector space is formed by Tamura texture features, gray-gradient symbiotic matrix, Hu invariant moment, and color moment of the image, a total of 28 characteristic parameters.

Among them, Tamura texture features theoretically include six components. But according to the Tamura feature extraction results of photoelectric fusion images, the characteristic parameters of Tamura texture features that are insensitive to photoelectric fusion images are ignored, and only the roughness, contrast, and directionality are used as features of pattern recognition. Then, 15 gray-gradient symbiotic matrix features, seven texture features, and three color moment features are, respectively, extracted to form the eigenvector space of the photoelectric fusion PD pattern [25–28].

However, there may be overlapping information between different features, resulting in multiple collinearity between the feature parameters. Meanwhile, too many dimensions of the feature vector can easily stress the training of the model, resulting in a lower recognition rate.

Therefore, in order to more fully characterize the characteristic information of the PD pattern and reduce the burden of the model, we use the principal component analysis (PCA) method to reduce the dimension of the eigenvector space. First, the factor correlation analysis of eigenvector space is carried out, gaining the value of KMO: 0.8356. The value of Bartlett spherical test is 132.96. It can be seen that there is strong partial correlation between feature vectors, which is suitable for dimensionality reduction by PCA [29]. In this study, according to the contribution rate of the feature factors, the first eight principal component factors with the cumulative contribution rate of 98% are selected as the input parameters of the recognition model. The PCA results are shown in Table 1.

**Table 1.** Contribution rate of principal component factors.

| Factor Number | 1 | 2 | 3 | 4 | 5 | 6 | 7 | 8 | 9 | 10 | ... | 28 |
|---|---|---|---|---|---|---|---|---|---|---|---|---|
| Contribution rate/% | 65.00 | 11.46 | 7.78 | 6.01 | 3.02 | 2.21 | 1.58 | 0.86 | 0.64 | 0.58 | ... | 0.01 |
| Cumulated contribution rate/% | 65.00 | 76.46 | 84.24 | 90.25 | 93.27 | 95.48 | 97.06 | 97.92 | 98.56 | 99.14 | ... | 100 |

### *4.5. Pattern Recognition Results of Different PD Patterns*

On the basis of the principal component factors described above, different classifiers are used to identify the PD experimental data. The classifiers used, in this study, were linear discriminant analysis (LDA) [30], k-nearest neighbor (KNN) [31], and support vector machine (SVM) algorithm [32]. LDA is a dimensionality reduction technology for supervised learning, which projects the sample onto a sorting line determining the category of the new sample based on the position of the projected point. KNN is a classification and regression method, which determines the classification by calculating which category of k-nearest samples in the feature space of a sample most belongs. The SVM algorithm maps points in low-dimensional space to high-dimensional spaces making them linearly separable, and then classifying them by the principle of linear partitioning.

In order to verify the applicability of the photoelectric fusion PD pattern proposed in this study, the above three classifiers were used to test the photoelectric fusion PD pattern samples, comparing with the recognition results of optical patterns and UHF patterns. At the same time, in order to verify the influence of different training sample numbers, four pattern recognition tests were carried out, respectively. In these four tests, the total number of training samples was 300, 240, 180, and 120, respectively, including all three types of defects. Therefore, the number of testing samples in these four tests were 60, 120, 180, and 240 correspondingly, including all three types of defects as well. It can be seen from the recognition results that different types of PD patterns have a significant influence on the recognition rate, as shown in Figure 16. The definition of recognition rate is:

$$Recognition\ rate\ = \frac{sample\ number\ of\ correct\ recognition}{number\ of\ testing\ sample}$$

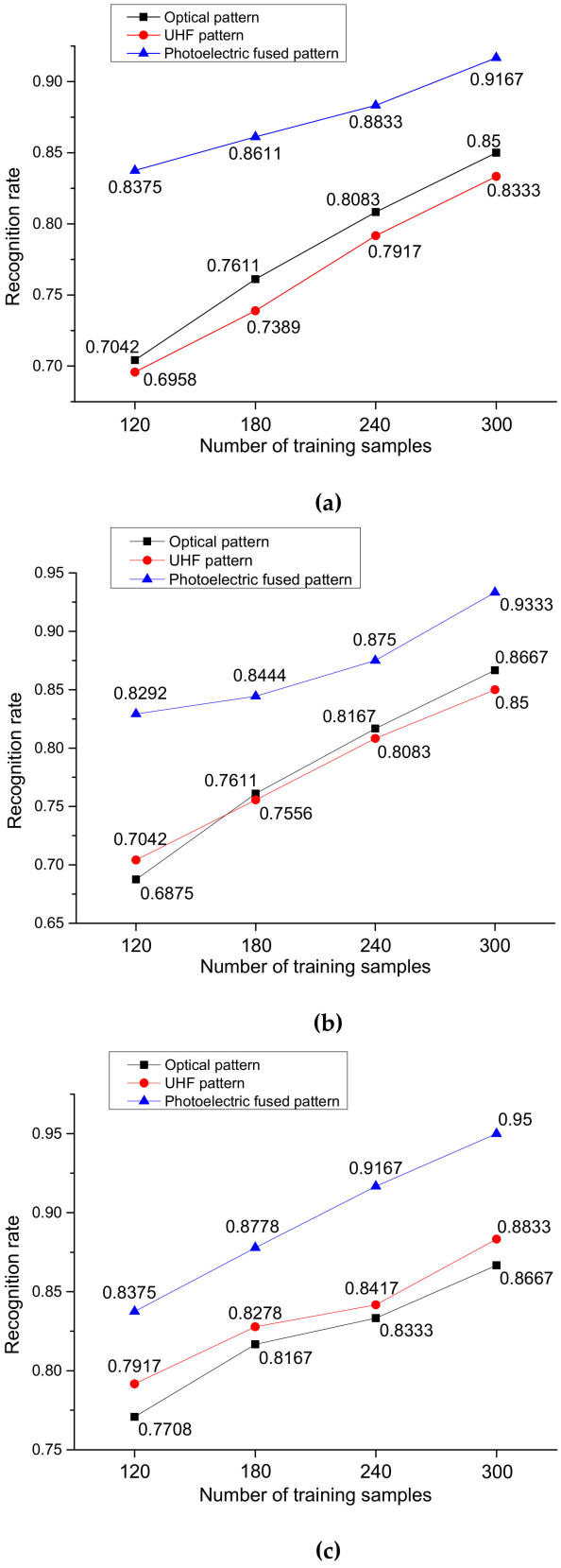


**Figure 16.** Recognition results of different classifiers. (**a**) linear discriminant analysis (LDA) classifier, (**b**) k-nearest neighbor (KNN) classifier, and (**c**) support vector machine (SVM) classifier.

According to Figure 16, the recognition rate of the photoelectric fusion pattern is the highest using any classifier. For all three types of PD patterns, the recognition rate increases with the increase of training samples. When using the SVM classifier with 300 training samples, the recognition rate of the photoelectric fusion pattern can reach up to 0.95. Moreover, the recognition rate of the photoelectric fusion pattern can still reach about 0.83 when the number of samples is only 120. Therefore, it can be concluded that the photoelectric fusion pattern can significantly improve the accuracy of PD pattern recognition.

In addition, when the number of training samples is the same, the accuracy of the recognition of the photoelectric fusion pattern by the three classifiers is higher than that of the optical pattern and the UHF pattern. Because photoelectric fusion pattern proposed in this study contains more abundant PD characteristic information, it can effectively improve the accuracy of the recognition. When the number of training samples is only 120, the average recognition rate of the three classifiers in each case is calculated in Figure 17, where three types of PD defects are, respectively, identified by different patterns. It can be seen that the recognition rate of the needle defect by the UHF pattern is especially low because of the loss of UHF signals. Moreover, the recognition rate of the free particle defect by the optical pattern is lower than the others because of the loss of optical signals. However, pattern recognition using photoelectric fusion pattern not only greatly increases the recognition rate of the needle defect and the free particle defect, but also slightly improves the recognition rate of the floating defect. Therefore, the proposed photoelectric fusion pattern has practicality.

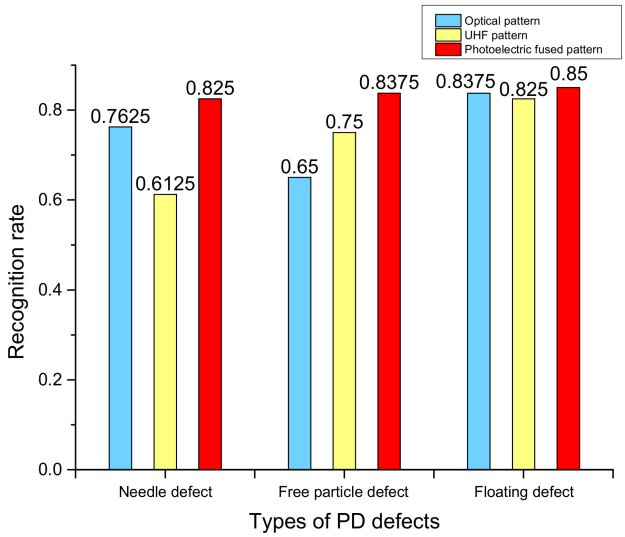


**Figure 17.** Average recognition rate of each defect under different kinds of patterns (with 120 training samples).

## 5. Conclusions

In this study, the optical-UHF integrated PD detection of GIL experimental platform is built, collecting PD patterns of three typical PD defects. Aiming at the PD pattern recognition problem of the GIL, an image fusion algorithm based on NSCT is proposed, which can fuse the optical PD pattern with the UHF PD pattern. Finally, three different classifiers are used to identify the photoelectric fusion PD pattern, which can verify the feasibility of this method. The conclusions are summarized as follows:

1) Due to the limitation of the PD detection principle and the influence of the GIL structure, the UHF pattern of the needle PD defect and the optical pattern of the free-particle PD defect have the loss of PD signals in the GIL. This phenomenon results in the reduction of the effective characteristic information in the PD pattern, which can reduce the pattern recognition accuracy of the PD.
2) The photoelectric fusion pattern can effectively avoid signals loss of UHF detection and optical detection in some situations, which can reduce the negative influence of false mode and pattern

aliasing on recognition. Through the photoelectric fusion pattern, the characteristic information of optical patterns and UHF patterns can complement each other, improving the accuracy and reliability of PD pattern recognition.

3) Compared with the optical pattern and the UHF pattern, the photoelectric fusion pattern can significantly improve the recognition rate of PD pattern recognition under the three kinds of classifiers, which can reach up to 0.95. In addition, when the number of training samples is small, the recognition rate can still reach about 0.83. Furthermore, the photoelectric fusion pattern not only greatly improves the recognition rate of the needle defect and the free particle defect, but the recognition accuracy of the floating defect can also be slightly improved. Therefore, the photoelectric fusion pattern has a good application effect.

**Author Contributions:** Data curation, Y.Z.; formal analysis, Y.Z.; funding acquisition, W.L.; methodology, Y.Z.; supervision, Y.Q., Y.X., G.S., and X.J.; writing—original draft, Y.Z.

**Funding:** This work was supported by the National Key R & D Program of China (2017YFB0902500) and the State Grid Science & Technology Project (the key technology of environment-friendly gas-insulated transmission line).

**Conflicts of Interest:** The authors declare no conflict of interest.

## References

1. Volcker, O.; Koch, H. Insulation co-ordination for gas-insulated transmission lines (GIL). *IEEE Trans. Power Deliv.* **2001**, *16*, 122–130. [CrossRef]
2. Magier, T.; Tenzer, M.; Koch, H. Direct Current Gas-Insulated Transmission Lines. *IEEE Trans. Power Deliv.* **2018**, *33*, 440–446. [CrossRef]
3. Miyazaki, A.; Takinami, N.; Kobayashi, S.; Yamauchi, T.; Hama, H.; Araki, T.; Nishima, H.; Hata, H.; Yamaguchi, H. Line constant measurements and loading current test in long-distance 275 kV GIL. *IEEE Trans. Power Deliv.* **2001**, *16*, 165–170. [CrossRef]
4. Schoffner, G. In A directional coupler system for the direction sensitive measurement of UHF-PD signals in GIS and GIL. In Proceedings of the 2000 Annual Report Conference on Electrical Insulation and Dielectric Phenomena (Cat. No.00CH37132), Victoria, BC, Canada, 15–18 October 2000; pp. 634–638.
5. Okubo, H.; Yoshida, M.; Takahashi, T.; Hoshino, T.; Hikita, M.; Miyazaki, A. Partial discharge measurement in a long distance SF/sub 6/gas insulated transmission line (GIL). *IEEE Trans. Power Deliv.* **1998**, *13*, 683–690. [CrossRef]
6. Li, J.; Han, X.; Liu, Z.; Yao, X. A Novel GIS Partial Discharge Detection Sensor With Integrated Optical and UHF Methods. *IEEE Trans. Power Deliv.* **2018**, *33*, 2047–2049. [CrossRef]
7. Han, X.; Li, J.; Zhang, L.; Pang, P.; Shen, S. A Novel PD Detection Technique for Use in GIS Based on a Combination of UHF and Optical Sensors. *IEEE Trans. Instrum. Meas.* **2019**, *68*, 2890–2897. [CrossRef]
8. Yongpeng, X.; Yong, Q.; Gehao, S.; Xiuchen, J.; Xiaoli, Z.; Zijie, W. Simulation analysis on the propagation of the optical partial discharge signal in I-shaped and L-shaped GILs. *IEEE Trans. Dielectr. Electr. Insul.* **2018**, *25*, 1421–1428. [CrossRef]
9. Cunha, A.L.D.; Zhou, J.; Do, M.N. The Nonsubsampled Contourlet Transform: Theory, Design, and Applications. *IEEE Trans. Image Process.* **2006**, *15*, 3089–3101. [CrossRef]
10. Wang, X.; Song, R.; Song, C.; Tao, J. The NSCT-HMT Model of Remote Sensing Image Based on Gaussian-Cauchy Mixture Distribution. *IEEE Access* **2018**, *6*, 66007–66019. [CrossRef]
11. Hanai, M.; Kojima, H.; Hayakawa, N.; Mizuno, R.; Okubo, H. Technique for discriminating the type of PD in SF6 gas using the UHF method and the PD current with a metallic particle. *IEEE Trans. Dielectr. Electr. Insul.* **2014**, *21*, 88–95. [CrossRef]
12. Ren, M.D.M.; Zhang, C.; Zhou, J. Partial Discharge Measurement under an Oscillating Switching Impulse: A Potential Supplement to the Conventional Insulation Examination in the Field. *Energies* **2016**, *9*, 623. [CrossRef]
13. Firuzi, K.; Vakilian, M.; Phung, B.T.; Blackburn, T.R. Partial Discharges Pattern Recognition of Transformer Defect Model by LBP & HOG Features. *IEEE Trans. Power Deliv.* **2019**, *34*, 542–550.

14. Mahyari, A.G.; Yazdi, M. Panchromatic and Multispectral Image Fusion Based on Maximization of Both Spectral and Spatial Similarities. *IEEE Trans. Geosci. Remote. Sens.* **2011**, *49*, 1976–1985. [CrossRef]
15. Yang, Y.; Tong, S.; Huang, S.; Lin, P. Multifocus Image Fusion Based on NSCT and Focused Area Detection. *IEEE Sens. J.* **2015**, *15*, 2824–2838.
16. Lei, T.; Feng, Z.; Zong-Gui, Z. In The nonsubsampled contourlet transform for image fusion. In Proceedings of the 2007 International Conference on Wavelet Analysis and Pattern Recognition, Beijing, China, 2–4 November 2007; pp. 305–310.
17. Bhatnagar, G.; Wu, Q.M.J.; Liu, Z. Directive Contrast Based Multimodal Medical Image Fusion in NSCT Domain. *IEEE Trans. Multimed.* **2013**, *15*, 1014–1024. [CrossRef]
18. Bhateja, V.; Patel, H.; Krishn, A.; Sahu, A.; Lay-Ekuakille, A. Multimodal Medical Image Sensor Fusion Framework Using Cascade of Wavelet and Contourlet Transform Domains. *IEEE Sens. J.* **2015**, *15*, 6783–6790. [CrossRef]
19. Shao, L.; Kirenko, I. Coding Artifact Reduction Based on Local Entropy Analysis. *IEEE Tran. Consum. Electron.* **2007**, *53*, 691–696. [CrossRef]
20. Jia-Shu, Z.; Cun-Jian, C. In Local variance projection log energy entropy features for illumination robust face recognition. In Proceedings of the 2008 International Symposium on Biometrics and Security Technologies, Islamabad, Pakistan, 23–24 April 2008; pp. 1–5.
21. Zhang, L.; Zhang, L.; Mou, X.; Zhang, D. FSIM: A Feature Similarity Index for Image Quality Assessment. *IEEE Trans. Image Process.* **2011**, *20*, 2378–2386. [CrossRef]
22. Li, H.; Qiu, H.; Yu, Z.; Zhang, Y. Infrared and visible image fusion scheme based on NSCT and low-level visual features. *Infrared Phys. Technol.* **2016**, *76*, 174–184. [CrossRef]
23. Zhu, Z.; Zheng, M.; Qi, G.; Wang, D.; Xiang, Y. A Phase Congruency and Local Laplacian Energy Based Multi-Modality Medical Image Fusion Method in NSCT Domain. *IEEE Access* **2019**, *7*, 20811–20824. [CrossRef]
24. Qu, X.-B.; Yan, J.-W.; Xiao, H.-Z.; Zhu, Z.-Q. Image Fusion Algorithm Based on Spatial Frequency-Motivated Pulse Coupled Neural Networks in Nonsubsampled Contourlet Transform Domain. *Acta Autom. Sin.* **2008**, *34*, 1508–1514. [CrossRef]
25. Amadasun, M.; King, R. Textural features corresponding to textural properties. *IEEE Trans. Syst. Man Cybern.* **1989**, *19*, 1264–1274. [CrossRef]
26. Tamura, H.; Mori, S.; Yamawaki, T. Textural Features Corresponding to Visual Perception. *IEEE Trans. Syst. Man Cybern.* **1978**, *8*, 460–473.
27. Weng, T.; Yuan, Y.; Shen, L.; Zhao, Y. In Clothing image retrieval using color moment. In Proceedings of the 2013 3rd International Conference on Computer Science and Network Technology, Dalian, China, 12–13 October 2013; pp. 1016–1020.
28. Soh, L.; Tsatsoulis, C. Texture analysis of SAR sea ice imagery using gray level co-occurrence matrices. *IEEE Trans. Geosci. Remote Sens.* **1999**, *37*, 780–795. [CrossRef]
29. Gonzalez-Audicana, M.; Saleta, J.L.; Catalan, R.G.; Garcia, R. Fusion of multispectral and panchromatic images using improved IHS and PCA mergers based on wavelet decomposition. *IEEE Trans. Geosci. Remote Sens.* **2004**, *4*, 1291–1299. [CrossRef]
30. Wei-Shi, Z.; Jian-Huang, L.; Yuen, P.C. GA-fisher: A new LDA-based face recognition algorithm with selection of principal components. *IEEE Trans. Syst. Man Cybern. Part B* **2005**, *35*, 1065–1078.
31. Xiong, J.; Zhang, Q.; Sun, G.; Zhu, X.; Liu, M.; Li, Z. An Information Fusion Fault Diagnosis Method Based on Dimensionless Indicators With Static Discounting Factor and KNN. *IEEE Sens. J.* **2016**, *16*, 2060–2069. [CrossRef]
32. Laufer, S.; Rubinsky, B. Tissue Characterization With an Electrical Spectroscopy SVM Classifier. *IEEE Trans. Biomed. Eng.* **2009**, *5*, 525–528. [CrossRef]